



Flat metasurfaces to collimate electromagnetic waves with high efficiency

HUA ZHU,¹ TAO XU,² ZHUO WANG,³ JUNHAO LI,¹ ZHIHONG HANG,^{2,6} LEI ZHOU,³ SHUQI CHEN,⁴ XUN LI,⁵ AND LIN CHEN^{1,*}

¹Wuhan National Laboratory for Optoelectronics, Huazhong University of Science and Technology, Wuhan 430074, China

²College of Physics, Optoelectronics and Energy and Collaborative Innovation Center of Suzhou Nano Science and Technology, Soochow University, Suzhou 215006, China

³State Key Laboratory of Surface Physics and Key Laboratory of Micro and Nano Photonic Structures (Ministry of Education), Fudan University, Shanghai 200433, China

⁴Laboratory of Weak Light Nonlinear Photonics Ministry of Education School of Physics, Teda Applied Physics Institute, Nankai University, Tianjin 300071, China

⁵Department of Electrical and Computer Engineering, McMaster University, 1280 Main Street West, Hamilton, Ontario, L8S 4L8, Canada

⁶zhhang@suda.edu.cn

*chen.lin@mail.hust.edu.cn

Abstract: Directional beaming of electromagnetic waves passing through a subwavelength aperture has attracted considerable interests in photonics, but the traditional approach of utilizing gratings to directionally couple surface waves (SWs) to a desired far-field direction faces the low-efficiency issue owing to high-order diffractions. Here we experimentally demonstrate that directional beaming of light can be realized with very high efficiencies, in which two specifically designed metasurfaces (MTSs) are placed at two sides of the aperture to serve as SW to propagating-wave meta-couplers. Different from the grating couplers, the well-designed phase-gradient meta-couplers can freely select the desired diffraction orders by suppressing the undesired diffraction orders. We design and fabricate MTSs with different phase gradients, and perform both far-field and near-field measurements to verify the predicted high-efficiency on/off-axis directional beaming effects. Experimental results are in good agreement with full wave simulations and theoretical analyses.

© 2018 Optical Society of America under the terms of the [OSA Open Access Publishing Agreement](#)

1. Introduction

According to the standard diffraction theory, light emerged from a subwavelength aperture will be diffracted in all directions uniformly. This property was long believed to be a fundamental constraint in manipulating light in a subwavelength scale for various technological requirements. In 2002, Ebbesen et al discovered that a subwavelength aperture in a metallic screen surrounded by periodic surface corrugations can realize directional beaming of light [1], i.e., light emitted from the subwavelength aperture will be redirected in a desired direction, instead of highly diverging in all directions. It is generally believed that the diffraction of surface plasmons on the surface corrugations or gratings gives rise to the beaming behavior [2–5]. The surface corrugations/gratings should not only support the propagation of the surface waves (SWs), but also serve as diffraction gratings to diffract the SWs along a desired direction by compensating the momentum mismatch between the radiation waves and the SWs. Since then, the utilization of surface corrugations/gratings for mediating SW diffraction has stimulated considerable interest in realizing diversified functionalities from visible to microwave regions including on/off-axis beaming [6–13], focusing [14,15], directional tunable beaming [16,17], and multiple directional beaming [18].

As the two-dimensional equivalence to metamaterials, metasurfaces (MTSs) have provided an unprecedented approach to the extreme control of electromagnetic waves (EWs)

by locally manipulating the phase, amplitude, and/or polarization of the scattered field. During the past years, much effort has been focused on using MTSs to control light propagation in free space, leading to a variety of applications including anomalous reflection/refraction [19–23], planar lens [24], vortex plates [25], high resolution holograms [26], ultrathin invisibility cloak [27,28], enhancement of nonlinear optical response [29,30], and coding MTS [31,32]. It has been experimentally demonstrated that MTSs can redirect an impinging light into the air along the one or more desired directions with high efficiency by suppressing the undesired grating diffractions [22,31,33]. The usage of gradient MTS to enable the conversion of the radiation wave into the SW was widely studied [34–36], however, less effort has been devoted to exploring the utilization of gradient MTS as a meta-grating to control directional re-radiation of the SW. The authors have proposed and numerically demonstrated the directional beaming of light in the optical domain by using gradient MTS to mediate the emerged light from a subwavelength aperture [37]. However, naively applying the concept of gradient MTS for directional beaming of light may yield low diffraction efficiency. The underlying reason for the low diffraction efficiency is that the MTS has not been well exploited to suppress the undesired diffraction orders, and thus, no comparative advantage over the conventional grating scheme has been implied. In this paper, we have demonstrated that well-designed MTS can significantly suppress the undesired diffraction orders, and hence significantly higher diffraction efficiency can be realized (77% in the experiment). In addition, we have made detailed explanation on why the MTS scheme shows superior advantage over the conventional grating one in terms of diffraction efficiency. As an illustration, we have designed and fabricated the directional beaming structures, and performed far-field measurement and near-field (NF) scanning experiments to characterize their excellent beaming performances. Different from the transmissive MTSs to steer the incident EWs [38,39], our proposal here is aimed at using gradient MTSs to mediate the emitted EWs from the subwavelength aperture along a desired direction.

2. Results and discussion

2.1 Design principle

Consider a SW mode propagating along a metallic grating that is typically used to surround a metallic aperture for light beaming [Fig. 1(a)]. As the SW mode propagates along the grating, it will be diffracted into radiation waves in the air with the radiation angle being determined by the grating diffraction equation, $k_{sw} - 2\pi m/p = k_0 \sin \theta$, where $k_{sw}(k_0)$ and p denote the propagation constant of the SW (radiation wave), and grating period, respectively, and m is an integer ($= 0, \pm 1, \pm 2, \pm 3 \dots$). For this scheme, one can't suppress any diffraction order to radiate the diffracted waves along a certain direction. Without loss of generality, we calculate the dependence of θ on the ratio of grating period and light wavelength, λ , [Fig. 1(b)] under the assumption that k_{sw} is equal to k_0 , in which actually k_{sw} is larger than k_0 in general. Figure 1(b) clearly presents that more and more diffraction orders appear as the grating period is increased. As an example, if p is assumed to be 2.4 times as large as λ , the guided SW mode will be diffracted into 4 beams of radiation waves, associated with 4 diffraction orders [Fig. 1(c)]. As a result, a significant portion of SW energy will be redirected into the undesired direction due to the presence of higher-order diffractions, leading to a low diffraction efficiency for directional beaming [10–13]. To ensure the maximum diffraction efficiency for directional beaming, it is highly desired that the SW mode is diffracted along a certain direction, rather than radiated along multiple directions. Therefore, the long-period gratings (larger than λ), corresponding to multiple-order grating diffraction, in principle prevent the formation of high-efficiency directional beam if they are used to mediate light emerged from a subwavelength aperture. It is therefore not surprising that the previous beaming systems typically suffer from low diffraction efficiency, especially for off-axis directional beaming where long-period gratings are indispensable for the design [10–13]. In the following work,

we will show how the gradient MTSs overcome the low efficiency issue faced by the conventional grating schemes.

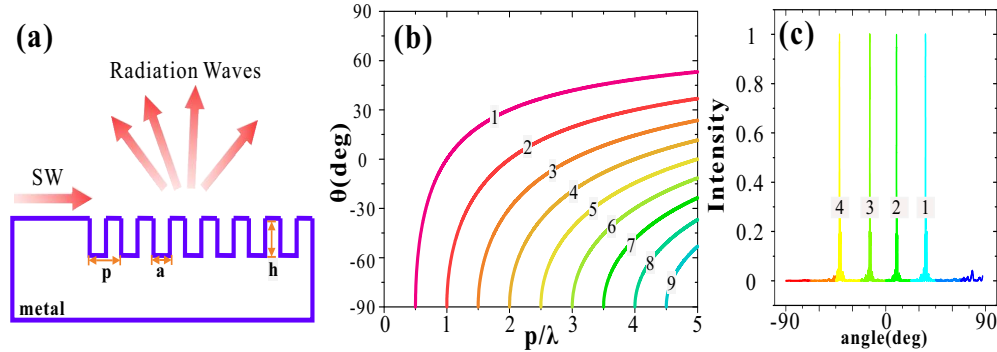


Fig. 1. (a) Schematic of a SW mode converted into radiation wave by a metallic grating. The grating period, depth and the width of air gap are denoted as p , h and a , respectively. (b) The radiation angle diffracted versus the ratio of the grating period and the wavelength in the air. (c) The normalized far-field intensity distributions as a function of the spatial angle when the SW ($k_{sw} \approx k_0$) propagate toward the grating with $h = 0.14\lambda$, $p = 2.4\lambda$ and $a = 0.11\lambda$. Here the metal is treated as perfect electrical conductivity in the microwave regime. The numbers in (b-c) represent the diffraction orders.

We start from analyzing the electromagnetic properties of the building block (meta-atom) of the MTS consisting of a metallic strip and a metal plate separated by a dielectric spacer [shown in the inset of Fig. 2(a)]. Figure 2(a) schematically shows a supercell of the MTS comprised of several different subunits. When the subunit structure is illuminated by x -polarized EWs, electric current will be generated on the metal strip and the ground metal plate simultaneously. Thus, strong magnetic field is generated inside the dielectric spacer due to the NF coupling. The phase of the reflected waves can be adjusted to an arbitrary value within 0 - 2π range by changing structural parameters. In this work, we firstly calculate the dependence of phase of reflected EWs on width w_x when the incident plane waves illuminate the subunit structures (not shown here). Then, we choose to vary the width of the metal strip, w_x , to enable the reflection-phase, φ , to cover 0 - 2π , so that a constant phase-gradient, $d\varphi/dx$, within a supercell is introduced. Therefore, the incident plane wave (with the incident angle θ_i) will receive an in-plane wave vector, $m2\pi/L_x$ (m is an integer), from the gradient-phase MTS, and the total transverse wave vector can be expressed as

$$k_x = k_0 \sin \theta_i + m2\pi / L_x \quad (1)$$

where k_0 represents the propagation constant in the air. Different from the conventional grating structure, the diffraction order of the MTS grating can be freely controlled by designing the phase gradient of the MTS to the desired value of $2m_1\pi/L_x$ (m_1 is the desired diffraction order). Besides, such periodical metallic strips on a metal plate can support a SW mode, with the propagation constant, k_{sw} , highly dependent on the geometrical parameters of the metallic strips. If k_x is not equal to the propagation constant, k_{sw} , the incident EW will be anomalously reflected back into the air. However, if k_x is exactly equal to k_{sw} , the incident EWs will be partially converted into the SW mode propagating along the MTS [Fig. 2(a)], and thus significantly enhanced absorption occurs. This can be noticeably reflected by the reflection curve versus the incident angles, where a reflection dip is supposed to appear at a certain θ_i , with k_x being exactly equal to k_{sw} . We have designed five sets of MTSs (A-E) that have $d\varphi/dx$ ($= 2\pi/L_x$) of $1.15k_0$, $0.94k_0$, $1.42k_0$, $0.71k_0$ and $1.65k_0$, respectively, at 7.5 GHz, to merely trigger the first diffraction order. For a supercell comprised of several subunits with different metal strip widths, w_x , as shown in Fig. 2(a), the k_{sw} of the SW mode can be theoretically retrieved by use of the transmission-line model [40]. As shown in Fig. 2(b), the

input impedance, Z_{in} , for the subunit structure is a parallel connection of the periodical metal strips impedance, Z_m , and the surface impedance of the dielectric spacer, Z_d , yielding the expression for x-polarized incidence wave [40]

$$Z_{in}^x = \frac{j\omega\mu_0 \frac{\tan(\beta d_1)}{\beta} \cos^2(\theta_2)}{1 - 2k_{eff} \alpha \frac{\tan(\beta d_1)}{\beta} \cos^2(\theta_2)} \quad (2)$$

where $k = k_0\sqrt{\epsilon_r}$, $\beta = \sqrt{k^2 - k_x^2}$, $k_{eff} = k_0\sqrt{(\epsilon_r + 1)/2}$, $\theta_2 = \arcsin[\sin(\theta_1)/\sqrt{\epsilon_r}]$, and $\alpha = -k_{eff} p_x / \pi \ln\{\sin[\pi(p_x - w_x)/2p_x]\}$, ϵ_r , μ_0 are the relative permittivity and the permeability of the dielectric spacer, respectively, and θ_1 , k_x are the incident angle and transverse wave vector of the incident EWs, respectively. Here we assume the loss of the dielectric spacer is sufficiently small so that it can be neglected. The propagation constants of the SW can be inferred under the transverse resonance condition [40]

$$Z_0^{-1} + (Z_{in}^x)^{-1} = 0 \quad (3)$$

where Z_0 is the free-space impedance for TM mode $Z_0 = \eta_0 \cos \theta$ ($\eta_0 = \sqrt{\mu_0 / \epsilon_0}$, ϵ_0 is the free-space permittivity). The incident angle, θ_i , can be extracted from $\cos \theta_i = \sqrt{(k_0^2 - k_x^2) / k_0}$. It should be noted that here k_x is the propagation constant of the SW and is larger than k_0 in general. The Z_{in}^x for each subunit structure can thus be retrieved by combining Eqs. (2) and (3). Finally, the input impedance for a supercell can be deemed as the average impedance for all subunit structures

$$\overline{Z_{in}^x} = \frac{1}{n} \sum_{i=0}^n (Z_{in}^x)_i \quad (4)$$

The k_{sw} of the MTS can be retrieved by incorporating Z_{in}^x into Eq. (2). The calculated dispersion relations for the five MTSs (A-E) are presented in Fig. 2(c). We can thus easily get the incident angles for the five MTSs (0.20°, 13.6°, -14.8°, 28.0° and 30.6° for A-E, respectively) at 7.5GHz by incorporating the retrieved k_{sw} into Eq. (1), in which the incident EWs are resonantly converted into the SW. The five incident angles are 0.20°, 13.6°, -14.8°, 28.0° and -30.6° for MTSs A-E, respectively, and are represented by the five-pointed stars shown in Fig. 2(d). To justify the validity of the theoretical prediction, we have performed finite difference time domain (FDTD) method to simulate the angle-reflection curves for MTSs A-E. As can be seen from Fig. 2(d) that, the five MTSs indeed have their own reflection dips associated with θ_i , which agrees well with the theoretical results (five-pointed stars) from transmission-line model described above. The propagation constants of the SW mode for the five MTSs are estimated as $1.15k_0$, $1.19k_0$, $1.18k_0$, $1.21k_0$ and $1.15k_0$, respectively. Figure 2(e) confirms that the radiation waves are coupled to the SW mode propagating along the surface of MTS A with the normal incidence. In contrast to the normal incidence, when the EWs illuminate MTS A with the incident angle of -20°, they are anomalously reflected with the radiation angle of -54.3° [Fig. 2(f)], consistent with the result from the generalized Snell's law [19].

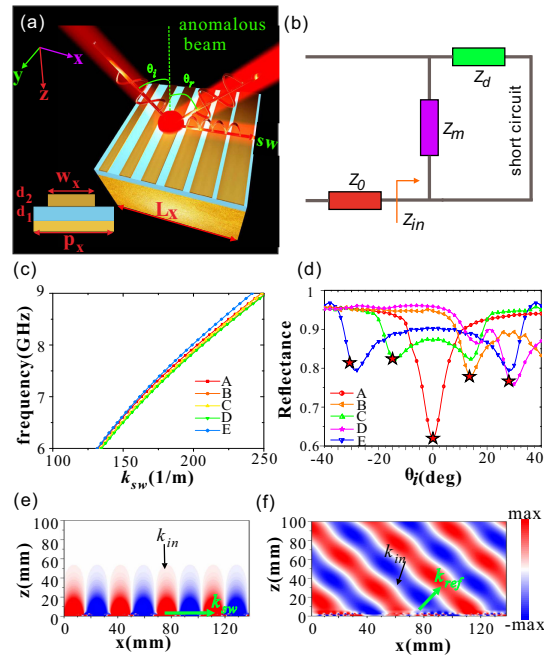


Fig. 2. (a) A supercell of the MTSs contains several subunits, each of which is comprised of a metal strip (yellow) and a metal plate separated by a dielectric spacer (light green). The lattice constant along x direction is denoted as L_x , the period of the subunit and width of the strip along x direction is represented by p_x and w_x , respectively, the thickness of the dielectric spacer, and the metal strip is denoted as d_1 , d_2 , respectively. $L_x = np_x$, with n indicating number of strips in a supercell. (b) Transmission line model for the subunit structures described by lumped impedances. (c) Dispersion relation curves for the MTSs A-E. (d) The dependence of the total power reflectance on the incident angles with x -polarized EMWs at 7.5 GHz illuminating the MTSs A-E. In the simulations, d_1 , d_2 for different MTSs are fixed at 1.8 and 0.018 mm, respectively, while the other structural parameters are given in Table 1. Cu and FR4 are selected as the metal layer and dielectric spacer, respectively. The conductivity of copper is $\sigma = 5 \times 10^7 (\Omega\text{m})^{-1}$ and the relative permittivity of FR4 is $\epsilon_r = 4.3 + 0.025i$ in the frequency range considered. The five-pointed stars denote the retrieved angles from the transmission-line model. (e, f) Simulated E_z field pattern on x - z plane when x -polarized EWs illuminate MTS A with the incident angle of 0° and -20° , respectively. All the simulations are conducted by a commercial software Lumerical finite difference time domain (FDTD) Solutions.

Table 1. Structural parameters for the five supercells

No.	n	p_x (mm)	L_x (mm)	w_x in each supercell (mm)
A	7	4.95	34.65	0.25, 4.22, 4.48, 4.61, 4.72, 4.82, 4.90
B	7	6.05	42.35	0.25, 4.83, 5.23, 5.42, 5.58, 5.77, 5.99
C	5	5.60	28	0.25, 4.78, 5.08, 5.27, 5.55
D	8	7	56	0.25, 5.15, 5.68, 5.94, 6.13, 6.33, 6.61, 6.95
E	4	6.05	24.2	0.25, 5.16, 5.5, 5.83

In view of the principle of optical path reversibility, the SWs can also be converted into the radiation waves redirected along the direction predicted by Eq. (1). It thus can be highly anticipated that the field distributions of the EWs emitted from a subwavelength aperture is significantly mediated by the MTSs surrounding the aperture. The proposed beaming structure is schematically shown in Fig. 3, where a subwavelength metal aperture is surrounded by the MTSs on both sides. When a beam of x -polarized EWs illuminate the metal plate from the bottom, a portion of the emitted EWs are coupled to the SW mode propagating both left- and right-ward along the MTS, while the remaining EWs are directly diffracted into air uniformly. Meanwhile, the SWs will firstly induce the magnetic resonance of each subunit and then be scattered by the MTS and retransferred to the radiation waves

with the radiation angle being determined by the MTSs used. The field distributions in the output space can thus be reconstructed due to the interference between the EWs scattered by the MTS and directly emitted out from the aperture. In order to realize directional beaming effect, the EWs scattered by the MTS on the left- and right sides should radiate along the same direction so that they can interfere constructively in the output space. According to the generalized Snell's law, the transverse wave vectors at the two interfaces must satisfy the relation as [19]

$$k_0 \sin \theta_r - k_i \sin \theta_i = d\varphi / dx \quad (5)$$

where θ_r and k_i represent the reflection angle and the wave vector of the incident waves, respectively. For our case, the incident waves are the SWs with the propagation direction being parallel to the metal plate, i.e., $\theta_i = 90^\circ$. Consequently, the generalized Snell's law for the left- and right sides can be written as

$$\begin{cases} d\varphi_L / dx - k_{sw}^L = k_0 \sin \theta_L & (\text{left}) \\ k_{sw}^R - d\varphi_R / dx = k_0 \sin \theta_R & (\text{right}) \end{cases} \quad (6)$$

where $d\varphi_L / dx$ ($d\varphi_R / dx$), k_{sw}^L (k_{sw}^R), and θ_L (θ_R) are the phase-gradient, propagation constant of the SW, and diffraction angle for the left (right) MTS, respectively. To realize on-axis directional beaming ($\theta_L = \theta_R = 0^\circ$), it is required that the MTSs used on both sides should be symmetrically arranged to provide the phase gradients with equal amplitude but opposite directions ($d\varphi_L / dx = k_{sw}^L$ and $d\varphi_R / dx = k_{sw}^R$) [Fig. 3(a)]. As for the off-axis directional beaming ($\theta_L = \theta_R \neq 0^\circ$), one has to ensure that the phase-gradient of the MTSs on the left- and right sides have different amplitudes and opposite directions [Figs. 3(b) and 3(c)]. The well-designed MTS A can be used for the on-axis directional beaming, while a combination of MTSs B and C (or D and E) can be exploited to implement off-axis directional beaming. Substituting k_{sw} and the phase gradients of the MTSs on both sides into Eq. (6), we can estimate the beaming angles for the three cases of 0° [Fig. 3(a)], 15° [Fig. 3(b)], and 30° [Fig. 3(c)], respectively.

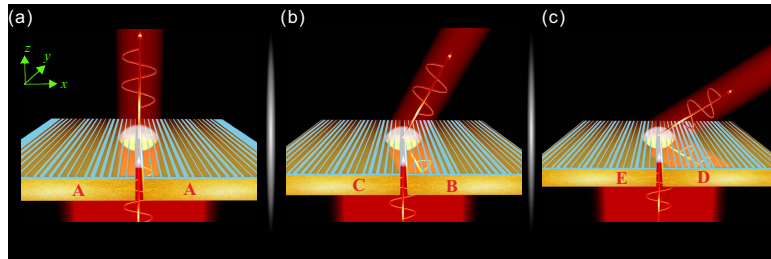


Fig. 3. Schematic of the directional beaming configurations: (a) MTS A is symmetrically arranged around the subwavelength aperture, and (b, c) MTS C (E) and B (D) are asymmetrically placed on the left- (C, E) and right (B, D) sides of the subwavelength aperture, respectively.

2.2 Simulation and experimental verification

To validate the directional beaming effect mentioned above, we employed FDTD simulations to calculate the field intensity distributions in the output space as the designed beaming structures are illuminated by normal-incidence plane waves from the bottom. The aperture of the beaming structures is centered at $x = 0$ and $z = 0$. The calculated field distributions of $|E|^2$ for the three cases [shown in Fig. 3] at 7.5GHz are presented in Figs. 4(a)-4(c). It can be observed that the emitted EWs from the apertures are redirected as directional beams in all cases. The radiation angles, well consistent with those predicted by theoretical analyses, are

highly dependent on the MTSs used. Figures 4(d)-4(f) show the E_z field distributions in the regions on the right side of the aperture, which confirms the excitation of the SW mode on the metallic surfaces. The effective wavelengths of their SW modes can be estimated by calculating the distance between two wave peaks, and the results agree well with those estimated from the theoretical analyses and angle-reflection curves in Figs. 2(c) and 2(d).

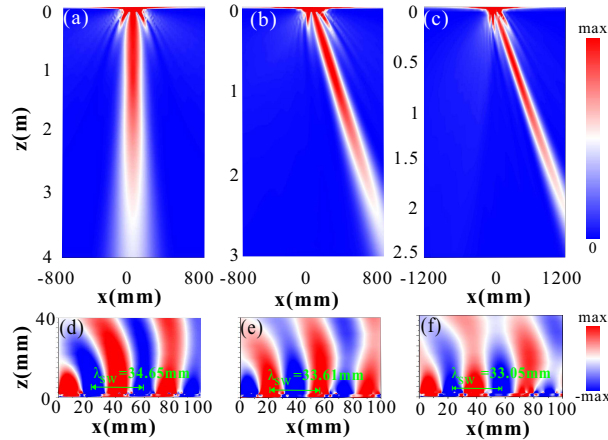


Fig. 4. (a-c) The simulated field intensity distributions of $|E|^2$ at 7.5 GHz when the first [Fig. 3(a)], second [Fig. 3(b)], and third [Fig. 3(c)] directional beaming configurations are illuminated from the bottom of the subwavelength aperture (4 mm width), respectively. In the simulations, 10, 8, 12, 6, and 14 supercells of MTS A, B, C, D, and E, respectively, are used. The other structural parameters of the MTSs are the same as those used in Fig. 2. (d-f) The zoom-in E_z field pattern corresponding to (a-c), respectively, in the regions on the right side of the aperture.

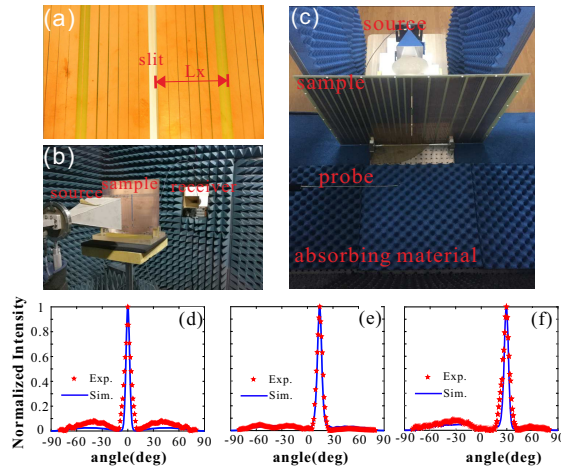


Fig. 5. (a) The schematic of the samples for on-axis directional beaming. The sizes for all the three fabricated samples are 700 mm \times 600 mm. (b, c) The experimental setup for the far-field measurement and NF scanning experiment, respectively. (d-f) The simulated (blue lines) and measured (red stars) far-field intensity profiles as a function of the spatial angle for the three samples, respectively.

We employed print circuit board technique to fabricate realistic samples [Fig. 5(a)], and performed far-field measurement [Fig. 5(b)], and NF scanning technique [Fig. 5(c)] to characterize the device performances. In the far-field experiments, the samples are placed vertically between a standard gain horn antenna and a receiving antenna [Fig. 5(b)]. The samples and the source gain horn antenna can be flexibly rotated with respect to the receiving antenna. The receiving antenna is 1.2 m away from the samples to receive the angular

spectrum. Both the antennas are connected to a vector network analyzer (Agilent E8362C PNA). The simulated and measured far-field intensity profiles versus the spatial angle for the three samples at 7.5GHz are presented in Figs. 5(d)-5(f). For the three cases, the simulated beaming angles of 0° , 14.6° and 29.8° , full width at half maximum (FWHM) of the far-field intensity is 5.0° , 5.9° and 5.8° , and the diffraction efficiency is 78%, 81%, and 74%, respectively [Figs. 5(d)-5(f)]. Here, the diffraction efficiency is defined as the percentage of incoming power distributed in the central beam of angular spectrum confined by the angles of two closely adjacent minimum [41]. The measured beaming angles of 0° , 14° , and 30° , FWHM of 6.2° , 6.9° , and 7.4° , and the diffraction efficiency of 67%, 77%, and 69%, respectively, for the three samples at 7.5 GHz are all well consistent with the FDTD simulation results. All the presented results indicate that the directional beaming effect with a small divergence angle and high efficiency is achievable with the MTS. To further confirm the formation of the directional beam, we conducted NF scanning experiments to observe the field intensity distributions in the output space. In the NF scanning experiments, the incident EWs are generated by a horn antenna [Fig. 5(c)]. In the far-field measurement and NF scanning experiments, the EWs emerged from the metallic silt can be treated as a secondary wavelet, and hence, the resultant measurement results will not be affected by the distance between the source horn antenna and the sample used for both measurements. A monopole antenna in the output space is used to detect the electric field. The measured resolution is set to be 5 mm per step both along x and z directions. Vector network analyzer (Keysight E5071C) is used for data acquisition. Part of the NF distributions are shown due to the limitation of translational stage used in the experiment. The position of the aperture is at $x = 0$ and $z = 0$. Figures 6(a)-6(c) show the simulated field intensity distributions of $|E|^2$ for the three beaming structures at 7.5 GHz. The measured patterns are shown in Figs. 6(d)-6(f) with the beaming angles of 0° , 14.5° , and 30° , which are all in excellent agreement with the simulated patterns in Figs. 6(a)-6(c), far-field angular field intensity profiles in Figs. 5(d)-5(f), and theoretical prediction.

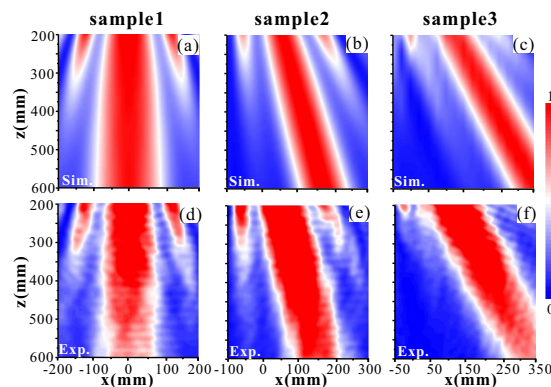


Fig. 6. The simulated (a-c) and measured (d-f) field intensity distributions of $|E|^2$ at 7.5 GHz, for the three samples, respectively.

The far-field and NF results mentioned above have demonstrated that, collimating EWs with high diffraction efficiency is achievable with gradient-phase MTSs. To make a meaningful comparison with previous grating-based beaming structures in terms of diffraction efficiency, we assume both of the beaming schemes work with the equivalent beaming angle of 30° . We designed three typical grating-based beaming structures [Figs. 7(a)-7(c)] to clearly explain how the grating period affects the resultant diffraction efficiency of directional beaming. In Figs. 7(a) and 7(b), merely one-side of gratings are used with grating A [with $p = 0.63\lambda$ in Fig. 7(a)] and with grating B [with $p = 1.82\lambda$ in Fig. 7(b)], while a combination of gratings A and B on both sides is employed in Fig. 7(c). It can be clearly observed from Fig. 7(d) that, the EWs after passing through the subwavelength aperture are

mainly diffracted into the designed angle of 30° once grating A is involved. Although grating A (grating period less than λ) on the left side works efficiently to diffract the left-side EWs into the desired direction, the total diffraction efficiency is limited to 26% as the EWs on the right side (no grating used) are uniformly diffracted with no directivity. As for grating B (grating period more than λ), the far-field intensity are almost uniformly distributed into three diffraction orders with the angles of 30° , -2.6° , and -37.13° , respectively. Consequently, the diffraction efficiency (9%) for the desired directional beam is even lower compared to Fig. 7(a). We note that a lot of schemes on off-axis light beaming were implemented by using two gratings of different periods on both sides of the aperture [10–13], i. e., grating A and grating B are used as schematically shown in Fig. 7(c). We emphasize here, the diffraction efficiency for the desired directional beaming is still low (28%) as a significant portion of diffracted EWs contribute to the second- and third-order diffractions due to the involvement of long-period grating B. As has been mentioned above, the diffraction efficiency for the directional beaming with MTSs can reach approximately 80%, suggesting significant superiority over the grating scheme. Two MTSs with different lattice constants, L_x , are used on one side of the aperture for the equivalent beaming angle of 30° , i. e., MTS E [with $L_x = 0.61\lambda < \lambda$ in Fig. 7(e)], and MTS D with [with $L_x = 1.4\lambda > \lambda$ in Fig. 7(f)], while a combination of MTSs E and D is used in Fig. 7(g). Similar to the short-period grating A, MTS E works efficiently to diffract EWs towards the beaming angle of 30° [Fig. 7(h)], though the total diffraction efficiency is relatively low (46%) as no MTS is used on the right side. What make the MTS superior to the grating is that, by setting the phase gradient $d\phi/dx$ to $2\pi/L_x$, a MTS with long lattice constant can significantly suppress the higher diffraction order ($m > 1$) so as to merely trigger the first diffraction order. As can be seen from Fig. 7(h) that, most of the EWs are directed into 30° with MTS D, while the far-field intensity for the second order with diffraction angle of -10.2° is notably lower and the diffraction efficiency (47%) is much higher than that with long-period grating B as shown in Fig. 7(b). Therefore, it can be reasonably expected to achieve significantly higher diffraction efficiency (74%) by connecting MTSs E and D, as opposed to the double-grating scheme in Fig. 7(c).

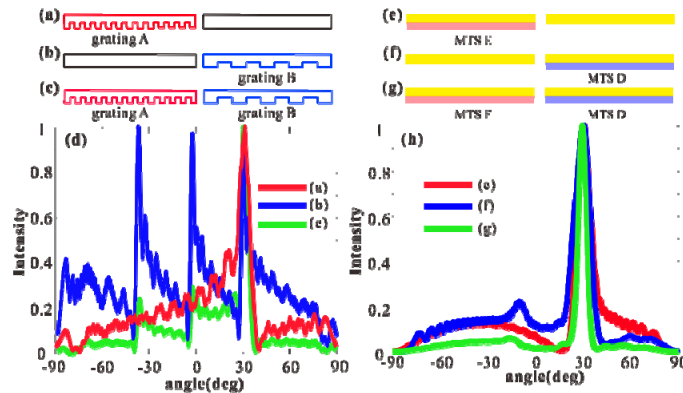


Fig. 7. (a-b) Short- (A) and long-period (B) gratings are placed on the left and right side of the metallic aperture, respectively. (c) Short- (A) and long-period (B) gratings are simultaneously arranged on both sides of the aperture. (d) The far-field intensity profiles as a function of the spatial angle at 7.5 GHz for (a-c). The structural parameters for grating A(B) is set with $h = 5.80$ (5.80) mm, $p = 72.75$ (25.11) mm, $a = 4.40$ (4.40) mm. (e-f) A metal aperture is surrounded by MTS E on the left side and by MTS D on the right side, respectively. (g) MTS E and by MTS D are simultaneously arranged on both sides of the aperture. (h) The far-field intensity profiles as a function of the spatial angle at 7.5 GHz for (e-g).

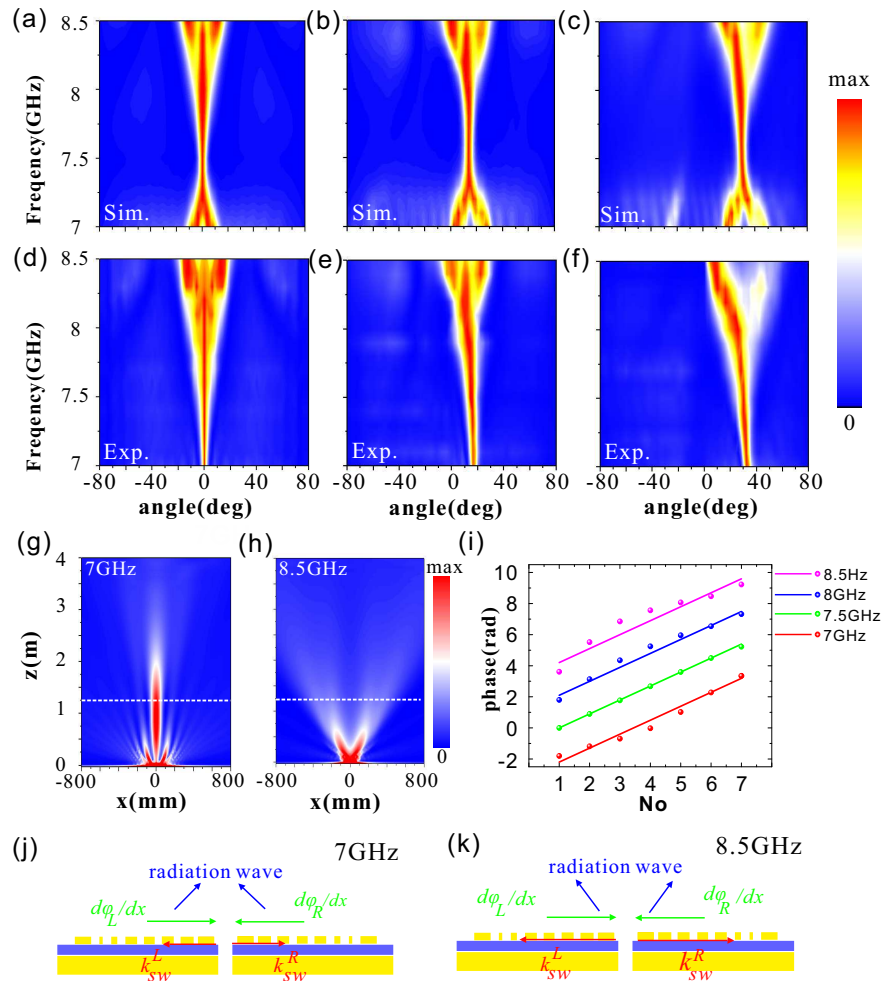


Fig. 8. Normalized far-field intensity as a function of the frequency and the spatial angle: (a-c) FDTD simulations and (d-f) experimental measurements for the three cases. (g, h) The simulated field intensity distributions of $|E|^2$ for the first beaming structure (Fig. 3a) at 7 GHz and 8.5GHz, respectively. The white dashed lines represent the positions of the receiving horn antenna. (i) The simulated (dots) and linearly fitted (solid lines) phase distributions within a supercell of metasurface A at different frequencies. (j,k) Schematics of the radiation direction of the EWs diffracted by the MTSS at 7 GHz and 8.5 GHz, respectively.

Although we only show the directional beaming effect at a single frequency of 7.5 GHz in Figs. 4-6, the operation bandwidth of the desired beaming effect can reach a few tenths of 1 GHz. To evaluate the operation bandwidth, we simulated the far-field intensity profiles with varied operation frequencies, and pictured the far-field intensity distributions as a function of working frequency and spatial angle in [Figs. 8(a)-8(c)]. It can be seen that the diffracted field spreads with a larger divergent angle if the working frequency deviates from the pre-designed frequency of 7.5 GHz. It should be emphasized here that the estimated working bandwidths for the three cases can reach up to 0.61, 0.65, and 0.54 GHz, respectively, with the criterion of the FWHM strictly below 10° . The measured far-field intensity distributions as a function of working frequency and spatial angle [Figs. 8(d)-8(f)] present excellent agreements with the simulation results above 7.5 GHz. However, the measured far-field intensity distributions below 7.5 GHz show much smaller divergent angle than that of 7.5 GHz. Due to the limitation of our microwave chamber, the receiving antenna can only be placed at a maximal distance of 1.2 m to the samples. In other words, the presented results shown in Figs. 8(d)-8(f)

could not really reflect the far-field intensity distributions at low frequencies. To more clearly explain the deviation, we have shown the field intensity distributions in the output space at 7 and 8.5 GHz in Figs. 8(g) and 8(h), at which the divergent angles present the largest difference with that at the pre-designed frequency of 7.5 GHz. Although the far-field diffraction patterns are both diverging at 7 and 8.5 GHz, the reason of the diverging effect is totally different. The beaming structure behaves like a focusing lens at 7 GHz so that the EWs are firstly redirected to a focal point and re-diverge afterward [Fig. 8(g)]. On the contrast, it acts as a beam splitter at 8.5 GHz that the emitted EWs radiate along two opposite spatial angles with respect to the central axis [Fig. 8(h)]. We emphasize here, to accurately reflect the far-field divergence, the receiving horn antenna should be placed at least a distance of 4 m to the samples. However, in the far-field measurement [Fig. 5(b)], the receiving horn antenna was placed a distance of 1.2 m from the samples [white dashed lines of Figs. 8(g) and 8(h)] due to the limited experimental space. The measured divergence angles are thus significantly less than the true values as presented by the simulation results. The dual-functionality at 7 and 8.5 GHz can be understood as follows. k_{sw} increases (decreases) if a higher (lower) working frequency is chosen [Fig. 2(c)], while the phase gradient is nearly unchanged [Fig. 8(i)]. As a result, the diffracted beam on both sides will be redirected towards the central axis at 7 GHz [Fig. 8(j)], leading to a focusing effect [Fig. 8(g)]. Meanwhile, the diffracted beam will be radiated away from the central axis at 8.5 GHz [Fig. 8(k)], resulting in a diverging effect [Fig. 8(h)].

3. Conclusion

We show that high-efficiency directional beaming can be realized by surrounding a subwavelength aperture with ultrathin flat MTSs on both sides. The MTS not only can support the propagation of the SWs, but also can enable SW to radiate along a well-desired direction determined by the geometrical parameters of the MTSs. The directional beaming effect is principally formed as a result of constructive interference between the EWs scattered by the MTS and directly emitted out from the aperture. We designed and fabricated the beaming structures, and characterized their beaming performances with far-field measurement and NF scanning experiment. Distinct from the previous corrugation/grooves structures, the present beaming scheme can notably increase the diffraction efficiency for the directional beam by significantly suppressing the high-order diffractions. The measured diffraction efficiency of the directional beam is approximately 77%, 69% if the beaming angle shifts to 14° , 30° , respectively, significantly superior to the long-period grating schemes. Besides, the proposed MTS beaming structures are about a thickness of $1/21$ working wavelength, much thinner than previously proposed grating-based beaming structures working in the same spectral region [7–9]. We have noted that a class of plasmonic lenses made of metal gratings that are capable of producing multiple free-space beams in arbitrary directions when a point source of SWs is located at the focus [42]. Similarly, such a MTS-based beam structures can also be expected to achieve multiple free-space beams by using metal antennas [22,37] instead of metal strips to surround a metal hole to scatter the SWs, which is our next plan. Finally, we believe that the proposal can be extended to operate in the optical wavelengths by scaling down the structural parameters, and can also lead to many other transmissive functional devices such as focusing lens and beam splitters.

Funding

National Natural Science Foundation of China (NSFC) (11104093, 11474116, 11574226, 11674068, 11734007); Natural Science Foundation of Jiangsu Province (BK20170058); National Basic Research Program of China (2017YFA0303504); Shanghai Science and Technology Committee (16JC1403100); State Key Laboratory of Advanced Technology for Materials Synthesis and Processing (Wuhan University of Technology).

References

1. H. J. Lezec, A. Degiron, E. Devaux, R. A. Linke, L. Martin-Moreno, F. J. Garcia-Vidal, and T. W. Ebbesen, "Beaming light from a subwavelength aperture," *Science* **297**(5582), 820–822 (2002).
2. L.-B. Yu, D.-Z. Lin, Y.-C. Chen, Y.-C. Chang, K.-T. Huang, J.-W. Liaw, J.-T. Yeh, J.-M. Liu, C.-S. Yeh, and C.-K. Lee, "Physical origin of directional beaming emitted from a subwavelength slit," *Phys. Rev. B Condens. Matter Mater. Phys.* **71**(4), 041405 (2005).
3. S. Carretero-Palacios, O. Mahboub, F. J. Garcia-Vidal, L. Martin-Moreno, S. G. Rodrigo, C. Genet, and T. W. Ebbesen, "Mechanisms for extraordinary optical transmission through bull's eye structures," *Opt. Express* **19**(11), 10429–10442 (2011).
4. A. Degiron and T. Ebbesen, "Analysis of the transmission process through single apertures surrounded by periodic corrugations," *Opt. Express* **12**(16), 3694–3700 (2004).
5. L. Martin-Moreno, F. J. Garcia-Vidal, H. J. Lezec, A. Degiron, and T. W. Ebbesen, "Theory of highly directional emission from a single subwavelength aperture surrounded by surface corrugations," *Phys. Rev. Lett.* **90**(16), 167401 (2003).
6. J.-M. Yi, A. Cuche, E. Devaux, C. Genet, and T. W. Ebbesen, "Beaming visible light with a plasmonic aperture antenna," *ACS Photonics* **1**(4), 365–370 (2014).
7. S. S. Akarca-Biyikli, I. Bulu, and E. Ozbay, "Enhanced transmission of microwave radiation in one-dimensional metallic gratings with subwavelength aperture," *Appl. Phys. Lett.* **85**(7), 1098–1100 (2004).
8. S. Cakmakyan, H. Caglayan, A. E. Serebryannikov, and E. Ozbay, "Experimental validation of strong directional selectivity in nonsymmetric metallic gratings with a subwavelength slit," *Appl. Phys. Lett.* **98**(5), 051103 (2011).
9. S. S. Akarca-Biyikli, I. Bulu, and E. Ozbay, "Resonant excitation of surface plasmons in one-dimensional metallic grating structures at microwave frequencies," *J. Opt. A, Pure Appl. Opt.* **7**(2), S159–S164 (2005).
10. S. Kim, H. Kim, Y. Lim, and B. Lee, "Off-axis directional beaming of optical field diffracted by a single subwavelength metal slit with asymmetric dielectric surface gratings," *Appl. Phys. Lett.* **90**(5), 051113 (2007).
11. Y. Yuan, J. Liu, J. He, and J. Yao, "Directional terahertz beams realized by depth-modulated metallic surface grating structures," *J. Opt. Soc. Am. B* **28**(11), 2674–2679 (2011).
12. H. Caglayan, I. Bulu, and E. Ozbay, "Observation of off-axis directional beaming via subwavelength asymmetric metallic gratings," *J. Phys. D Appl. Phys.* **42**(4), 045105 (2009).
13. F. Hao, R. Wang, and J. Wang, "A design methodology for directional beaming control by metal slit–grooves structure," *J. Opt.* **13**(1), 015002 (2011).
14. S. Kim, Y. Lim, H. Kim, J. Park, and B. Lee, "Optical beam focusing by a single subwavelength metal slit surrounded by chirped dielectric surface gratings," *Appl. Phys. Lett.* **92**(1), 013103 (2008).
15. J. Lee, K. Lee, H. Park, G. Kang, D.-H. Yu, and K. Kim, "Tunable subwavelength focusing with dispersion-engineered metamaterials in the terahertz regime," *Opt. Lett.* **35**(13), 2254–2256 (2010).
16. H. Kim, J. Park, and B. Lee, "Tunable directional beaming from subwavelength metal slits with metal-dielectric composite surface gratings," *Opt. Lett.* **34**(17), 2569–2571 (2009).
17. X. Song, N. Wang, M. Yan, C. Lin, J. Förstner, and W. Yang, "Direction-tunable enhanced emission from a subwavelength metallic double-nanoslit structure," *Opt. Express* **25**(12), 13207–13214 (2017).
18. Y. Liu, H. Shi, C. Wang, C. Du, and X. Luo, "Multiple-directional beaming effect of metallic subwavelength slit surrounded by periodically corrugated grooves," *Opt. Express* **16**(7), 4487–4493 (2008).
19. N. Yu, P. Genevet, M. A. Kats, F. Aieta, J.-P. Tetienne, F. Capasso, and Z. Gaburro, "Light propagation with phase discontinuities: generalized laws of reflection and refraction," *Science* **334**(6054), 333–337 (2011).
20. Z. Li, E. Palacios, S. Butun, and K. Aydin, "Visible-frequency metasurfaces for broadband anomalous reflection and high-efficiency spectrum splitting," *Nano Lett.* **15**(3), 1615–1621 (2015).
21. Z. Liu, Z. Li, Z. Liu, J. Li, H. Cheng, P. Yu, W. Liu, C. Tang, C. Gu, J. Li, S. Chen, and J. Tian, "High-performance broadband circularly polarized beam deflector by mirror effect of multianorod metasurfaces," *Adv. Funct. Mater.* **25**(34), 5428–5434 (2015).
22. S. Sun, K.-Y. Yang, C.-M. Wang, T.-K. Juan, W. T. Chen, C. Y. Liao, Q. He, S. Xiao, W.-T. Kung, G.-Y. Guo, L. Zhou, and D. P. Tsai, "High-efficiency broadband anomalous reflection by gradient meta-surfaces," *Nano Lett.* **12**(12), 6223–6229 (2012).
23. M. Kang, T. Feng, H.-T. Wang, and J. Li, "Wave front engineering from an array of thin aperture antennas," *Opt. Express* **20**(14), 15882–15890 (2012).
24. F. Aieta, P. Genevet, M. A. Kats, N. Yu, R. Blanchard, Z. Gaburro, and F. Capasso, "Aberration-free ultrathin flat lenses and axicons at telecom wavelengths based on plasmonic metasurfaces," *Nano Lett.* **12**(9), 4932–4936 (2012).
25. P. Genevet, N. Yu, F. Aieta, J. Lin, M. A. Kats, R. Blanchard, M. O. Scully, Z. Gaburro, and F. Capasso, "Ultra-thin plasmonic optical vortex plate based on phase discontinuities," *Appl. Phys. Lett.* **100**(1), 013101 (2012).
26. B. Walther, C. Helgert, C. Rockstuhl, F. Setzpfandt, F. Eilenberger, E. B. Kley, F. Lederer, A. Tünnermann, and T. Pertsch, "Spatial and spectral light shaping with metamaterials," *Adv. Mater.* **24**(47), 6300–6304 (2012).
27. X. Ni, Z. J. Wong, M. Mrejen, Y. Wang, and X. Zhang, "An ultrathin invisibility skin cloak for visible light," *Science* **349**(6254), 1310–1314 (2015).
28. Y. Yang, L. Jing, B. Zheng, R. Hao, W. Yin, E. Li, C. M. Soukoulis, and H. Chen, "Full-polarization 3D metasurface cloak with preserved amplitude and phase," *Adv. Mater.* **28**(32), 6866–6871 (2016).

29. N. Segal, S. Keren-Zur, N. Hendler, and T. Ellenbogen, "Controlling light with metamaterial-based nonlinear photonic crystals," *Nat. Photonics* **9**(3), 180–184 (2015).
30. O. Wolf, S. Campione, A. Benz, A. P. Ravikumar, S. Liu, T. S. Luk, E. A. Kadlec, E. A. Shaner, J. F. Klem, M. B. Sinclair, and I. Brener, "Phased-array sources based on nonlinear metamaterial nanocavities," *Nat. Commun.* **6**(1), 7667 (2015).
31. T. J. Cui, M. Q. Qi, X. Wan, J. Zhao, and Q. Cheng, "Coding metamaterials, digital metamaterials and programmable metamaterials," *Light Sci. Appl.* **3**(10), e218 (2014).
32. B. Xie, K. Tang, H. Cheng, Z. Liu, S. Chen, and J. Tian, "Coding acoustic metasurfaces," *Adv. Mater.* **29**(6), 163507 (2017).
33. S. Larouche and D. R. Smith, "Reconciliation of generalized refraction with diffraction theory," *Opt. Lett.* **37**(12), 2391–2393 (2012).
34. S. Sun, Q. He, S. Xiao, Q. Xu, X. Li, and L. Zhou, "Gradient-index meta-surfaces as a bridge linking propagating waves and surface waves," *Nat. Mater.* **11**(5), 426–431 (2012).
35. L. Huang, X. Chen, B. Bai, Q. Tan, G. Jin, T. Zentgraf, and S. Zhang, "Helicity dependent directional surface plasmon polariton excitation using a metasurface with interfacial phase discontinuity," *Light Sci. Appl.* **2**(3), e70 (2013).
36. W. Sun, Q. He, S. Sun, and L. Zhou, "High-efficiency surface plasmon meta-couplers: concept and microwave-regime realizations," *Light Sci. Appl.* **5**(1), e16003 (2016).
37. H. Zhu, X. Yin, L. Chen, and X. Li, "Directional beaming of light from a subwavelength metal slit with phase-gradient metasurfaces," *Sci. Rep.* **7**(1), 12098 (2017).
38. M. Decker, I. Staude, M. Falkner, J. Dominguez, D. N. Neshev, I. Brener, T. Pertsch, and Y. S. Kivshar, "High-efficiency dielectric Huygens' surfaces," *Adv. Opt. Mater.* **3**(6), 813–820 (2015).
39. C. Pfeiffer, N. K. Emani, A. M. Shaltout, A. Boltasseva, V. M. Shalaev, and A. Grbic, "Efficient light bending with isotropic metamaterial Huygens' surfaces," *Nano Lett.* **14**(5), 2491–2497 (2014).
40. O. Luukkonen, C. Simovski, G. Granet, G. Goussetis, D. Lioubtchenko, A. V. Raisanen, and S. A. Tretyakov, "Simple and accurate analytical model of planar grids and high-impedance surfaces comprising metal strips or patches," *IEEE Trans. Antenn. Propag.* **56**(6), 1624–1632 (2008).
41. J. Jiang, H. Wu, L. Jiang, and X. Li, "Genetic optimization of double subwavelength metal slits surrounded by surface dielectric gratings for directional beaming manipulation," *Opt. Commun.* **285**(8), 2201–2206 (2012).
42. J. Tetienne, R. Blanchard, N. Yu, P. Genevet, M. A. Kats, J. A. Fan, T. Edamura, S. Furuta, M. Yamanishi, and F. Capasso, "Dipolar modeling and experimental demonstration of multi-beam plasmonic collimators," *New J. Phys.* **13**(5), 053057 (2011).